

Terahertz Quantum Cascade Lasers, Electronics, and Real-time Imaging

Academic and Research Staff

Professor Qing Hu

Postdoctoral Associates

Benjamin S. Williams

Graduate Students

Hans Callebaut, Steve Kohen, Sushil Kumar, Alan Lee

Introduction

Millimeter-wave and THz frequencies ($f = 0.1\text{-}10$ THz) remain one of the most underdeveloped frequency ranges, even though the potential applications in remote sensing and imaging, spectroscopy, and communications are great. This is because the millimeter-wave and THz frequency range falls between two other frequency ranges in which conventional semiconductor devices are usually operated. One is the microwave frequency range, and the other is the near-infrared and optical frequency range. Semiconductor devices which utilize the classical diffusive transport of electrons, such as diodes and transistors, have a high frequency limit. This limit is set by the transient time and parasitic RC time constants. Currently, electron mobility and the smallest feature size which can be fabricated by lithography limit the frequency range to below several hundred GHz. Semiconductor devices based on quantum mechanical interband transitions, however, are limited to frequencies higher than those corresponding to the semiconductor energy gap, which is higher than 10 THz for most bulk semiconductors. Therefore, a large gap exists from 1 to 10 THz in which very few devices are available.

Semiconductor quantum-effect devices (which can be loosely termed "artificial atoms"), including both vertically grown quantum-well structures and laterally confined mesoscopic devices, are human-made quantum mechanical systems in which the energy levels can be chosen by changing the sizes of the devices. Typically, the frequency corresponding to the intersubband transitions is in the millimeter-wave range ($\Delta E \sim 1\text{-}4$ meV) for the lateral quantum-effective devices, and THz to infrared for the vertical quantum wells. It is therefore appealing to develop ultrahigh-frequency devices, such as THz lasers utilizing the intersubband transitions in these devices.

In our group, we are systematically investigating physical and engineering issues that are relevant to devices operating from millimeter-wave to THz frequencies. Specifically, we are working on THz quantum cascade lasers based on intersubband transitions in quantum wells, their applications as local oscillators in heterodyne receivers, and real-time THz imaging using focal-plane array cameras.

Development of terahertz quantum cascade lasers

Sponsors

National Science Foundation
Grant ECS-0217782
NASA
Grant NNG04GC11G
AFOSR
Grant F49620-00-1-0331
DOD NGSEG fellowship

Project Staff

Ben Williams, Hans Callebaut, Sushil Kumar, Steve Kohen, and Qing Hu, in collaboration with Dr. John Reno at Sandia National Lab.

Semiconductor quantum wells are human-made quantum mechanical systems in which the energy levels can be designed and engineered to be of any value. Consequently, unipolar lasers based on intersubband transitions (electrons that make lasing transitions between subband levels within the conduction band) were proposed for long-wavelength sources as early as the 1970s. However, because of the great challenge in epitaxial material growth and the unfavorable fast nonradiative relaxation rate, unipolar intersubband-transition lasers (also called quantum-cascade lasers) at mid-infrared wavelengths were developed only recently at Bell Laboratories. This achievement paved the way for development of coherent laser sources at customized frequencies ranging from THz to near-infrared. However, compared to the infrared QCLs, THz QCLs at much longer wavelengths face unique challenging issues. First, the energy levels corresponding to THz frequencies (1 THz = 4 meV) are quite narrow, so it is very challenging to design quantum well structures for selective injection to the upper level and selective depopulate electrons from the lower level. The requirements for fabrication of such quantum-well structures with adequate accuracies are also demanding. Because of the narrow separation between subband levels, heating and electron-electron scattering will have a much greater effect. Also, the small energy scales of THz photons make the detection and analysis of spontaneous emission (a crucial step toward developing lasers) quite difficult. Second, mode confinement, which is essential for any laser oscillation, is difficult at longer wavelengths. Conventional dielectric-waveguide confinement is not applicable because the evanescent field penetration, which is proportional to the wavelength and is on the order of several tens of microns, is much greater than the active gain medium of several microns. Recently (November 2002), we made a breakthrough in developing quantum-cascade lasers at 3.4 THz (corresponding to 87 μm wavelength). Since then, we have made rapid progress in developing many lasers with record performance, including but not limited to the highest pulsed operating temperature of 164 K, highest CW operating temperature of 117 K, and the longest wavelength of 141 μm (corresponding to 2.1 THz). Key results are summarized in the following sections.

THz quantum cascade lasers based on resonant phonon scattering for depopulation

The direct use of LO-phonon scattering for depopulation of the lower state offers several distinctive advantages. First, when a collector state is separated from the lower state by at least the phonon energy $\hbar\omega_{LO}$, depopulation can be extremely fast, and it does not depend much on temperature or the electron distribution. Second, the large energy separation provides intrinsic protection against thermal backfilling of the lower radiative state. Both properties are important in allowing higher temperature operation of lasers at longer wavelengths.

The present design combines advantages of our two previously investigated THz emitters. As shown in Fig. 1, the radiative transition between levels 5 and 4 is spatially vertical, yielding a large oscillator strength. The depopulation is highly selective, as only the lower level 4 is at resonance with a level 3 in the adjacent well, where fast LO-phonon scattering takes place. The four-well structure inside the dashed box is one module of the structure, and 175 such modules are connected in series to form the quantum cascade laser.

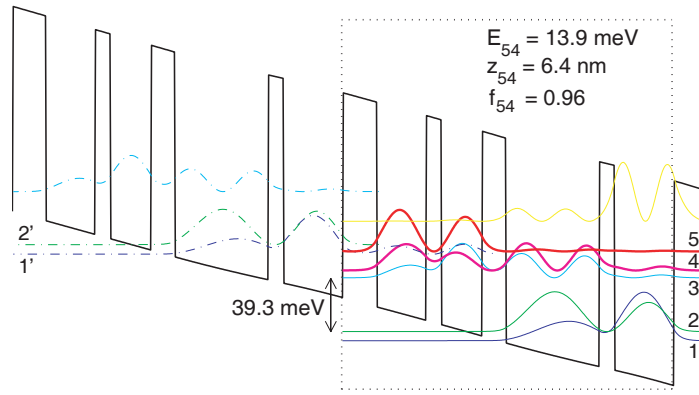


Figure 1. Conduction band profile calculated using a self-consistent Schrödinger and Poisson solver (80% conduction band offset) biased at 64 mV/module. Beginning with the injector barrier, the layer thickness in Å are **54/78/24/64/38/148/24/94**. The 148-Å well is doped with Si at $1.9 \times 10^{16}/\text{cm}^3$, yielding a sheet density of $2.8 \times 10^{10}/\text{cm}^2$.

Mode confinement in this laser device was achieved using a surface plasmon layer grown under the active region. The schematic of the device structure and the calculated mode profile and waveguide loss are shown in Fig. 2. The calculated waveguide loss of 7.1 cm^{-1} and mode confinement factor $\Gamma \approx 29\%$ are quite favorable compared to the calculated gain of our laser device.

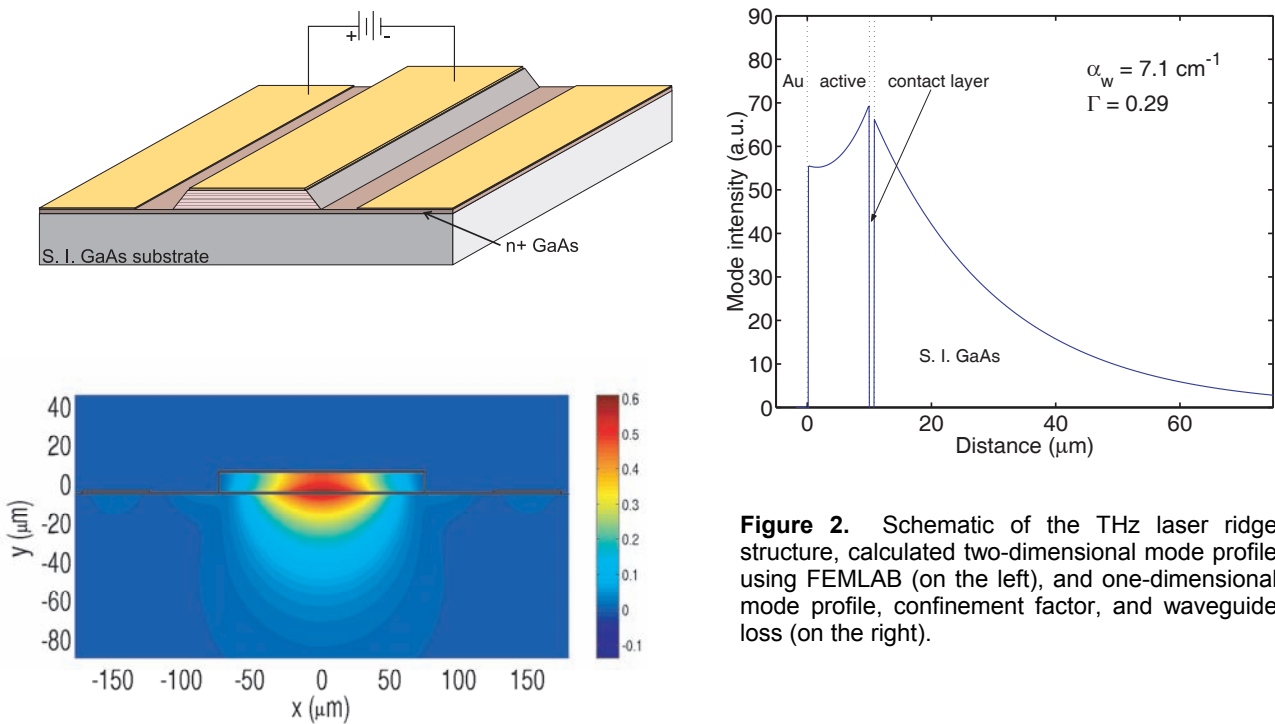


Figure 2. Schematic of the THz laser ridge structure, calculated two-dimensional mode profile using FEMLAB (on the left), and one-dimensional mode profile, confinement factor, and waveguide loss (on the right).

After the rear facet was high-reflection (HR) coated, lasing was obtained in this device and a typical emission spectrum above threshold is shown in Fig. 3(a). The emission frequency corresponds to a photon energy of 14.2 meV, close to the calculated value of 13.9 meV. Pulsed lasing operation is observed up to 87 K with a power level (measured using a calibrated thermopile detector, ScienTech Model #360203) of 13 mW at 5 K, and ~ 4 mW even at liquid-nitrogen temperature of 78 K, as shown in Fig. 3(b).

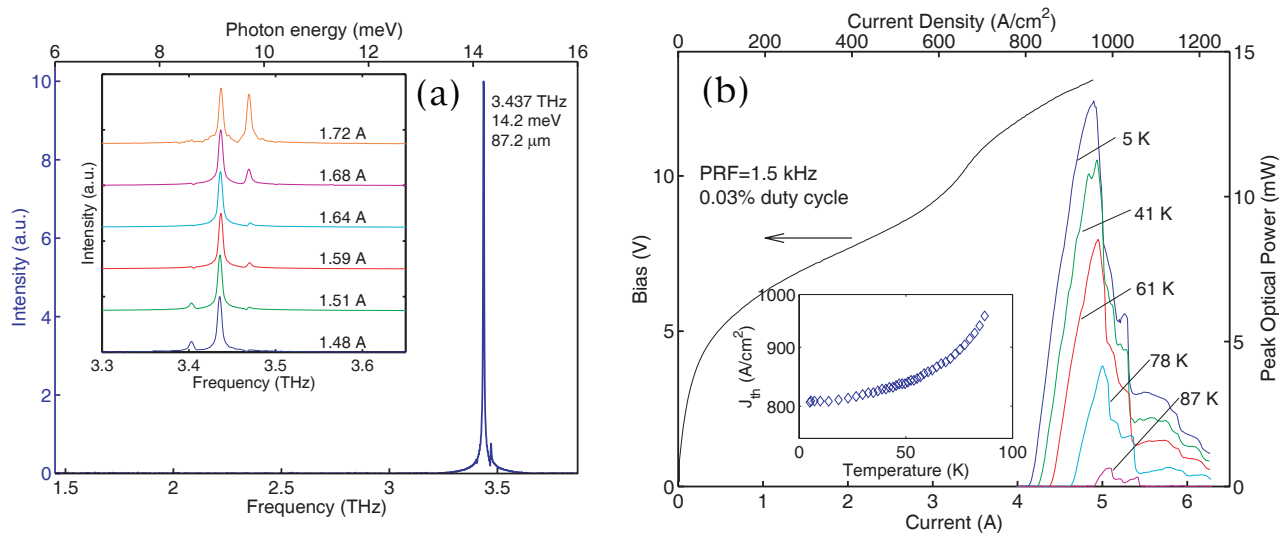


Figure 3. (a) Emission spectrum above threshold. The inset shows a set of emission spectra that are Stark-shifted to higher frequencies with higher bias. The linewidth is limited by the instrumental resolution of the FTIR ($0.125 \text{ cm}^{-1} = 3.75 \text{ GHz}$). (b) Pulsed power-current relations taken from a similar laser device at different heat-sink temperatures.

THz quantum cascade lasers using metal waveguides for mode confinement

After our initial success in the development of 3.4-THz quantum cascade laser, one of the improvements made was the mode confinement. As shown in Fig. 2, the mode confinement using surface plasmon layer yields a relatively low mode confinement factor of $\Gamma \approx 0.29$. This mode confinement is sufficient for lasing at 3.4 THz. However, as we are developing even longer wavelength quantum cascade lasers, the mode confinement will become much worse or even unconfined at frequencies lower than 2 THz for the carrier concentration in our laser structures. An alternative method for mode confinement is to use metal waveguides. As shown in Fig. 4, the mode is now tightly confined between the top and bottom metal contacts, yielding a confinement factor close to 100%. Fig. 4 also shows the process of wafer bonding and selective etching to fabricate such a metal waveguide structure.

Using a combination of the metal-metal waveguides and improved gain medium, we have developed THz QCLs with many record performance in the last year. Some of the highlights of these achievements are summarized in Fig. 5, including the highest operating temperature of 164 K in the pulsed mode (at this temperature $k_B T / \hbar \omega \approx 1.14$, which is unprecedented for any solid-state photonic devices), 117 K in CW mode, and the longest wavelength (141 μm , corresponding to 2.1 THz) QCL to date.

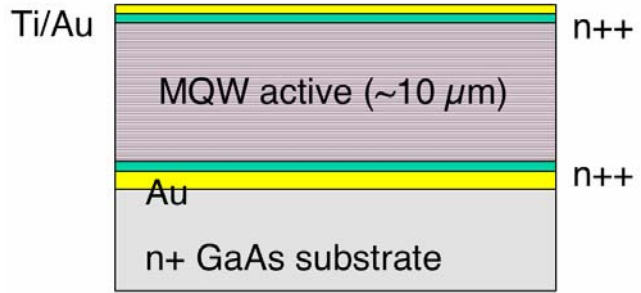
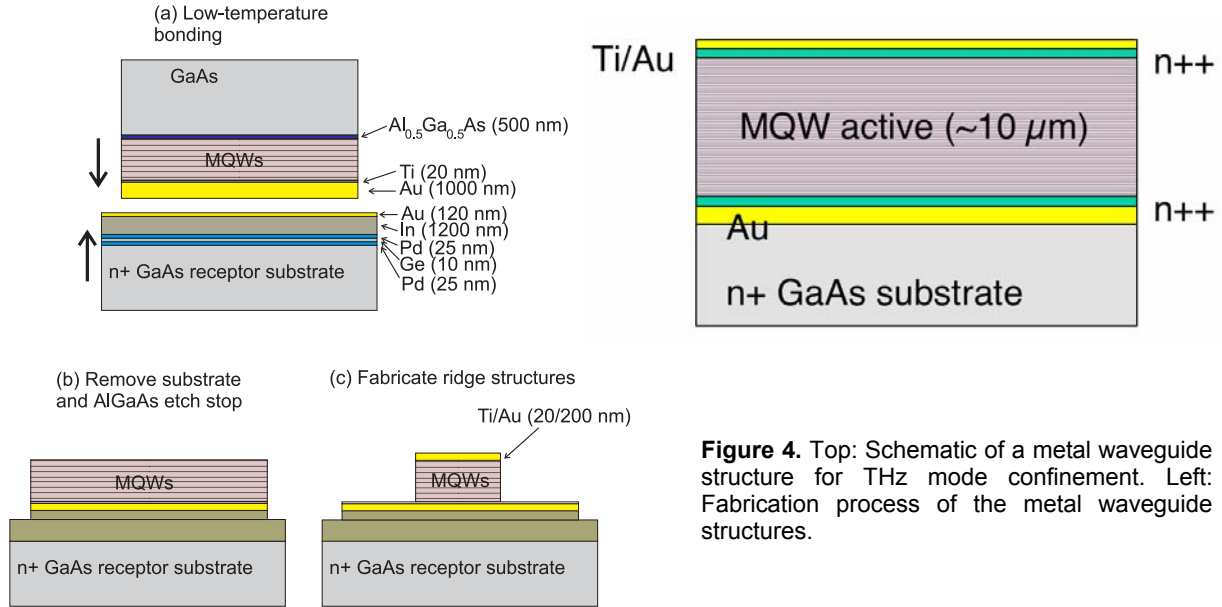


Figure 4. Top: Schematic of a metal waveguide structure for THz mode confinement. Left: Fabrication process of the metal waveguide structures.

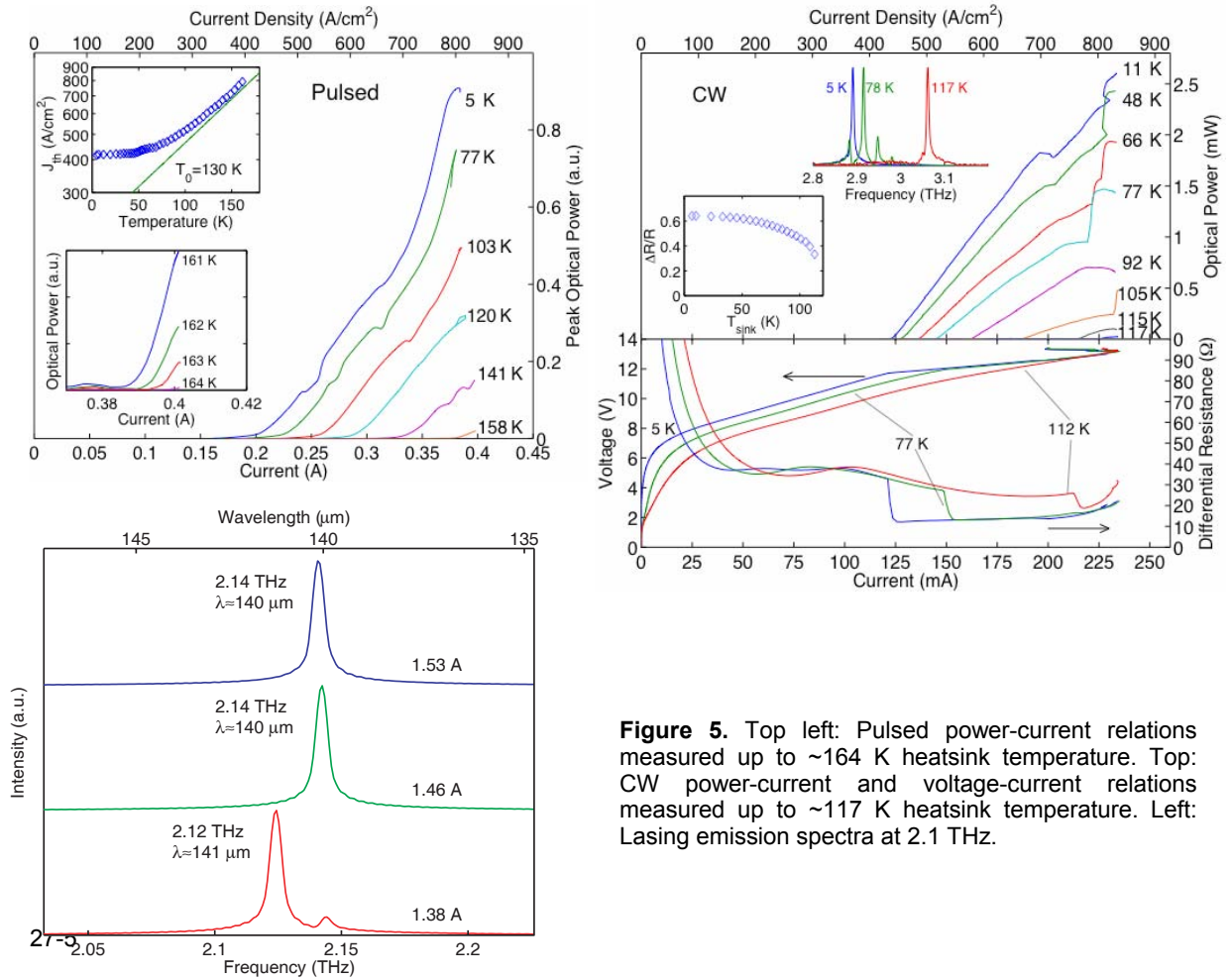


Figure 5. Top left: Pulsed power-current relations measured up to ~ 164 K heatsink temperature. Top: CW power-current and voltage-current relations measured up to ~ 117 K heatsink temperature. Left: Lasing emission spectra at 2.1 THz.

Analysis of transport properties of THz quantum cascade lasers

Sponsors

National Science Foundation
Grant ECS-0217782
NASA
Grant NNG04GC11G
AFOSR
Grant F49620-00-1-0331

Project Staff

Hans Callebaut, Ben Williams, Sushil Kumar, Qing Hu.

Even though mid-infrared and THz quantum cascade lasers operate on the same principle, that is, intersubband transition in semiconductor heterostructures, they show a qualitative difference in the dynamics of electron transport. For mid-infrared QCLs, the subband separations exceed the LO-phonon energy $\hbar\omega_{LO}$ and electron transport is dominated by LO-phonon scattering. For THz QCLs, many subband separations are smaller than $\hbar\omega_{LO}$, only the high-energy tail of a hot electron distribution is subject to the LO-phonon scattering, which results in a significantly higher temperature sensitivity for the electron transport and a far greater importance of electron-electron (e-e) scattering. The long delay in the development of THz QCLs is testimony to the difficulty of achieving population inversion involving these complicated transport mechanisms. It is thus important to quantitatively model these transport processes to extend the operation of THz QCLs to broader frequency ranges and higher temperatures.

Our transport analysis is based on Monte Carlo (MC) simulations, which have been used to analyze and design mid-infrared and THz QCLs. Compared to conventional rate-equation analysis, the MC method is especially useful for THz QCLs, as it does not rely on a specific model for carrier distributions and can easily handle temperature- and density-dependent scattering times. Fig. 6 illustrates the flow chart of our Monte Carlo simulation scheme. It follows a conventional scheme for an ensemble of particles, in our case 10^4 particles, with a focus on e-e and e-phonon interactions involving the electrons in one module of the device under study. An electron that scatters out of a module is reinjected with identical in-plane k -vector into a subband equivalent to its destination subband, in accordance with the spatial periodicity of QCLs.

The results of the Monte Carlo simulations, focused on the 3.4-THz laser structure shown in Fig. 1, are summarized in Fig. 7. All simulations assumed a lattice temperature of 25 K, corresponding to a 10 K heat sink temperature. In Fig. 8(a), the calculated I-V relation qualitatively resembles that of measured one, with the calculated peak current density is noticeable lower without including electron-impurity scattering. With the inclusion of electron-impurity scattering, the agreement is much better. The two horizontal lines are calculated total cavity losses with one facet Au coated and without any facet coating. Our device lased only with one facet coating, thus the two lines define the range of material gain in our laser device. The qualitative agreement between the MC and experimental results indicate the usefulness of MC simulation as a design tool.

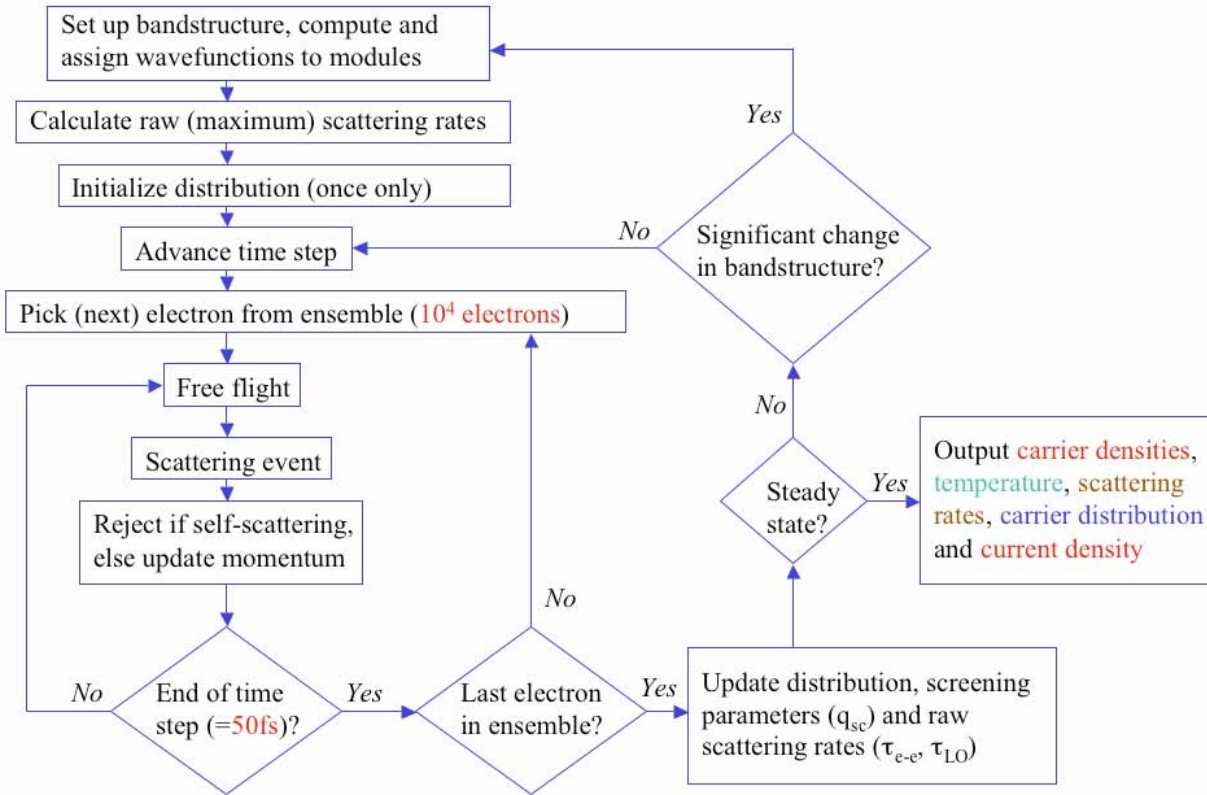


Figure 6. Flow chart of our ensemble Monte Carlo simulation scheme.

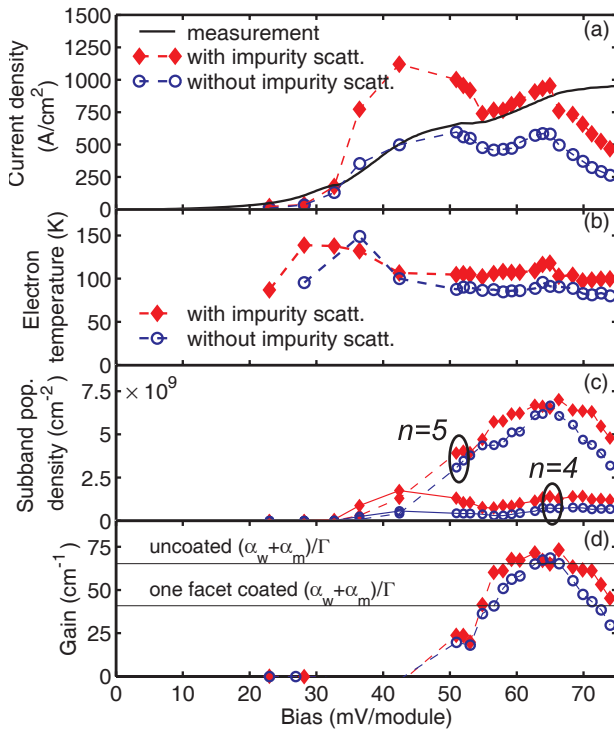


Figure 7. In (a)-(d), circle symbols are the results calculated without including electron-impurity scattering and diamond symbols are the results with electron-impurity scattering. (a) Current density for a range of biases. The injection anticrossing occurs at 65 mV/module. The measured current is represented as a full line. (b) Electron temperature T_e for the subbands involved in the radiative transition, $n = 4$ and $n = 5$. (c) The population density in $n = 4$ and $n = 5$. (d) Material gain for different biases. Also indicated are the calculated threshold gain values for a $1180 \times 150 \mu\text{m}^2$ ridge structure, with uncoated facets and with one facet HR coated.

Despite the reasonably good agreement shown in Fig. 7, however, a challenging problem remains in our transport analysis in how to deal with wavefunction localization caused by dephasing scattering. In all the MC studies on transport properties in QCL structures, the entire multiple quantum-well structure is treated as a single quantum mechanical system, for which Schrödinger's equation is solved to yield spatially extended subband states. In general, coherent interaction and time evolution is ignored, and transport is modeled as intersubband scattering among these spatially extended states, in a way similar to the Boltzmann transport equation. In this Boltzmann-like picture, potential barriers do not cause any bottlenecks in the transport process. For example, a thicker injection barrier only yields a smaller anticrossing gap, and thus will not affect the peak current density at resonance but will only makes the resonance sharper. In this picture, both the injection to the upper radiative level and removal of electrons from the lower radiative level tend to be quite efficient at resonance. As a result, our transport analysis based on this Boltzmann-like model predicted appreciable levels of gain in most of the structures that we have experimentally investigated for THz lasing. In real devices, however, dephasing scattering (due to interface roughness, alloy, and impurity scatterings) interrupts the coherent interactions between states and effectively localizes wavefunctions, making transport between weakly coupled states (characterized by a small anticrossing gap between these states) mostly an incoherent tunneling process. This incoherent sequential tunneling process is much less efficient than the injection and removal rates predicted by the Boltzmann-like model. A possible solution to deal with the problem of wavefunction localization is to start from a tight-binding model in a density-matrix formalism. In this model, the dephasing scattering damps the Rabi oscillation between two states across an energy barrier and therefore it comes in naturally in the reduction of the coupling/transport among spatially localized basis states. Another possible approach is based on a nonequilibrium Green's function theory, although not as intuitive as the MC approach, it takes all the dephasing processes into account and calculates important parameters such as the gain and current density. Both tasks are presently under our current investigations.

Electromagnetic modeling of terahertz quantum cascade laser waveguides and resonators

Sponsors

National Science Foundation
Grant ECS-0217782
NASA
Grant NNG04GC11G
AFOSR
Grant F49620-00-1-0331
DOD NGSEG fellowship

Project Staff

Steve Kohen, Ben Williams, and Qing Hu.

The design of optical confinement structure was a key development in the extension of QCLs from the mid-infrared regime to the longer-wavelength THz range. This was due, in part, to the difficulty in scaling the dimensions of conventional dielectric waveguides up with increasing wavelength as well as the increase in free-carrier loss (scaled as $\sim f^{-2}$) that occurs in the semiconductor cladding and active regions. In this project, we have used a commercial finite-element numerical simulator (FEMLAB) to analyze the properties of electromagnetic waveguides and resonators used in THz quantum-cascade lasers. Both metal-metal and semi-insulating (SI) surface plasmon ridge waveguide geometries were investigated. Simulations and analysis of two types were performed: two-dimensional waveguides (eigenmode calculation), and two- and three-dimensional resonators (facet reflectivity calculation for infinite width and finite width waveguides, respectively). Waveguide simulations extend previous transverse one-dimensional analyses to two dimensions (for the lateral and transverse dimensions), and quantify the breakdown of the one-dimensional approximation as the ridge width is reduced. Resonator simulations in two- and three-dimensions are performed and are used to obtain facet reflectivity and output radiation patterns. For the metal-metal waveguide structures, these resonator simulations quantitatively show strong deviation for terahertz facet reflectivity from those predicted by the effective index method. For the SI surface-plasmon waveguides, however, the effective index method for calculating reflectivity is still valid.

Investigation of THz quantum-cascade lasers using microprobe photoluminescence

Sponsors

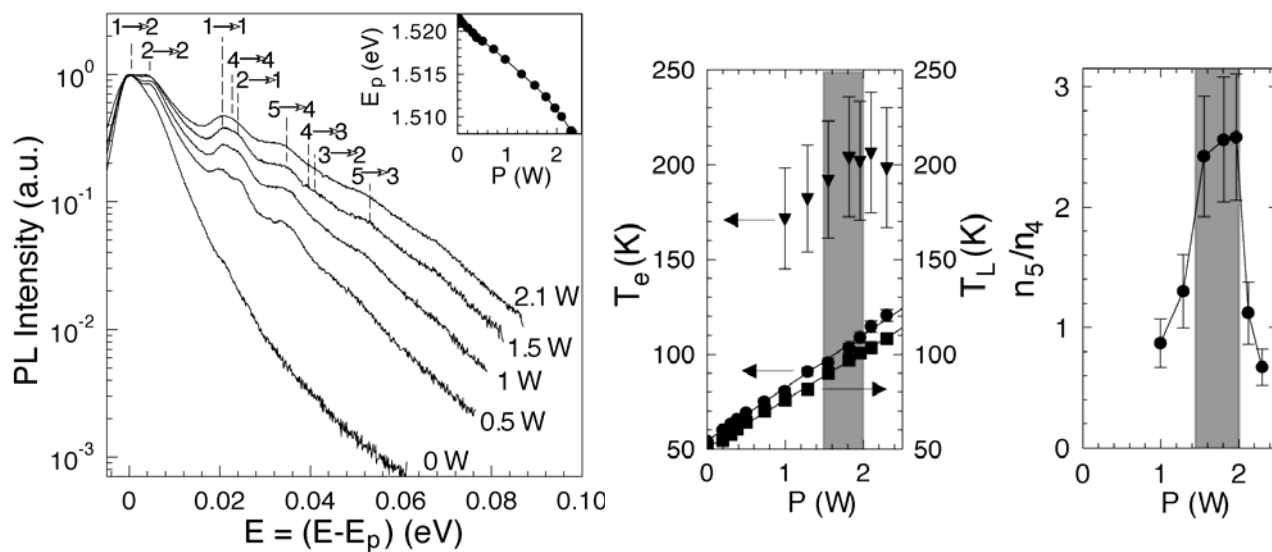
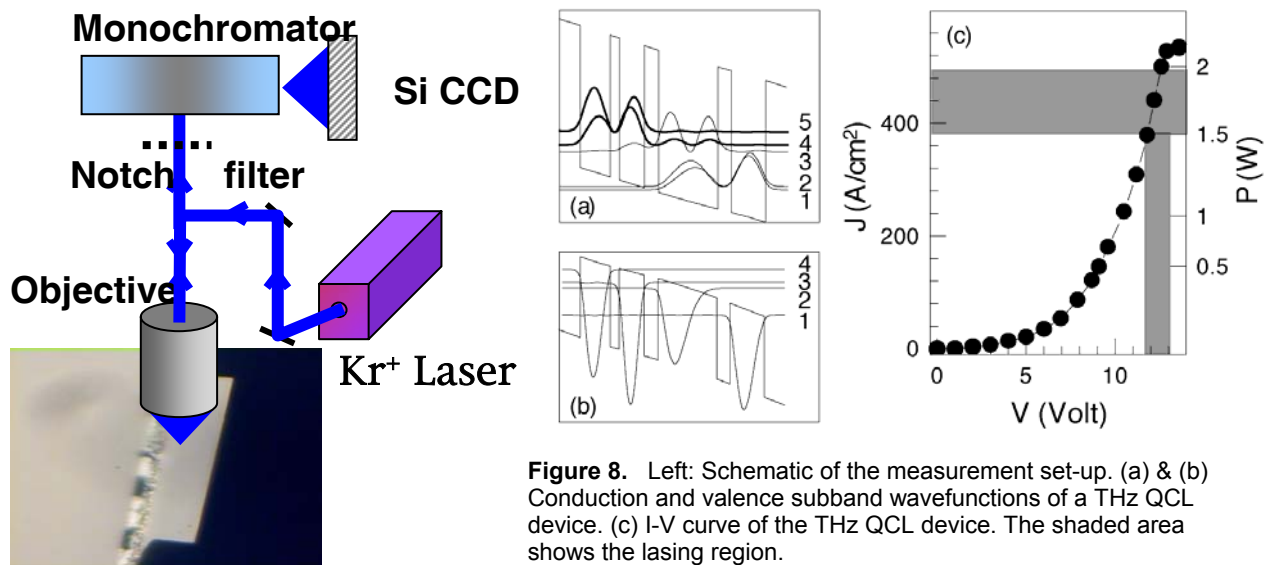
National Science Foundation
Grant ECS-0217782
NASA
Grant NNG04GC11G
AFOSR
Grant F49620-00-1-0331

Project Staff

Ben Williams, Sushil Kumar, Qing Hu, in collaboration with M. S. Vitiello, G. Scamarcio, and V. Spagnolo at INFM Regional laboratory and Università degli Studi di Bari, Italy, and Dr. John Reno at Sandia National Lab.

In this work we performed measurements of the electronic and lattice temperatures and the relative subband populations in resonant-phonon THz QCLs. The method used is microprobe photoluminescence (PL), with the schematic shown in Fig. 8. The importance of this information stems from the existence of non-equilibrium electronic distributions, characterized by temperatures higher than the lattice ones at injected currents close to the laser threshold. These hot electrons arise from the detailed balance between the injection rates and the main energy relaxation rates, i.e. inter- and intra-subband electron-electron, electron-LO phonon, electron-impurity, and interface roughness scattering. In THz QCLs, the photon energy is smaller than the longitudinal-optical (LO) phonon energy E_{LO} (36.6 meV in GaAs) and the electron-LO phonon scattering between radiative subbands is energetically forbidden at very low electronic temperatures (T_e). However, the strong T_e dependence of the nonradiative relaxation rate $\tau_{5 \rightarrow 4}^{-1} \propto \exp[(E - E_{LO})/k_B T_e]$ significantly reduces the gain and increases the threshold current density at high T_e . We show that optimizing the quantum design may improve the electron-lattice coupling and hence the electrical and optical performance of THz QCLs.

Figure 8 shows the schematic of the measurement set-up, along with the band profiles and I-V curve of a THz QCL device. Figure 9 shows a set of PL spectra for different values of the electrical power (P). The rich features in the spectra correspond to radiative transitions between different conduction and valence subbands, as indicated in the figure. From the areas of those peaks, subband population can be inferred; and from the slope of the spectra on the higher-energy side, the electron temperature of the involved subband can be deduced. These are important parameters for us to gain understanding of transport properties of the THz QCLs, in order to further optimize their performance. The results of electron temperatures and populations of the two radiative subbands (level 5 is the upper subband and level 4 is the lower one) are shown in Fig. 9. As expected, the electron temperature is substantially higher than the lattice temperature. Furthermore, the ratio of population n_5/n_4 shows a plateau in the bias region where the device lases, as required by the gain clamping for steady-state operations.



Terahertz heterodyne receiver using QCLs and hot-electron bolometers

Sponsors

National Science Foundation
Grant ECS-0217782
NASA
Grant NNG04GC11G
AFOSR
Grant F49620-00-1-0331

Project Staff

Ben Williams, Sushil Kumar, and Qing Hu, in collaboration with J.R. Gao, J. N. Hovenier, J. J. A. Baselmans, Z.Q. Yang, A. Baryshev, M. Hajenius, T. M. Klapwijk, A.J.L. Adam, and T.O. Klaassen at SRON National Institute for Space Research, and Kavli Institute of NanoScience Delft, Delft University of Technology, the Netherlands, and Dr. John Reno at Sandia National Lab.

The terahertz (THz) region of the electromagnetic spectrum (300 GHz – 10 THz) is the least explored spectral region in astronomy, despite the fact that it contains half the luminosity and 98% of the photons of the universe. This is mainly caused by the absence of sensitive detectors and the fact that the earth's atmosphere is opaque for large fractions of this spectral region. Ground, air and space based observatories are now starting to lift the veil but they are limited by the current state-of-the-art radiation detectors. In particular, there are no spectrometers capable of performing very high-resolution spectroscopy above 2 THz suitable for space-based observatories. Here we report the first demonstration of an *all* solid-state heterodyne receiver that can be used as such a spectrometer at frequencies above 2 THz. The system we present uses a hot electron bolometer as mixer and a quantum cascade laser as the local oscillator, operating at 2.8 THz, with an unprecedented combination of sensitivity and stability. The complete system provides a unique solution for THz spectroscopy for astronomy as well as Earth science.

Figure 10 shows a schematic view of the experimental setup with the QCL and the HEB mounted in two separate dewars. A wideband spiral antenna coupled NbN HEB mixer is used with a superconducting bridge of 4 μm wide, 0.4 μm long, and about 4 nm thick. The normal state resistance R_N of the device, measured above the critical temperature of about 9 K, is 65 Ω . Without radiation applied a critical current I_c of 320 μA is observed at 4.2 K. The radiation is coupled to the antenna using a standard quasi-optical technique: the Si chip with the HEB is glued to the back of an elliptical, anti-reflection coated Si lens. The lens is placed in a metal mixer block thermally anchored to the 4.2 K cold plate. The divergent beam from the QCL passes through a high-density polyethylene (HDPE) dewar-window and is collimated with a parabolic mirror. The radiation is further guided to the HEB dewar through a flat mirror and a 6 μm thick Mylar beam splitter, which acts as a directional coupler. A blackbody source (of Eccosorb) is used as the signal source, which defines a hot load at 295 K and a cold load at 77 K. The signal is combined with the QCL beam through the beam splitter. Both signals pass through the thin HDPE window and a metal mesh heat filter at 77 K of the HEB dewar. The IF signal, resulting from the mixing of the LO and the hot/cold load signal, is amplified using a low noise amplifier operated at 4.2 K, and is further fed to a room temperature amplifier and filtered at 1.4 GHz in a band of 80 MHz.

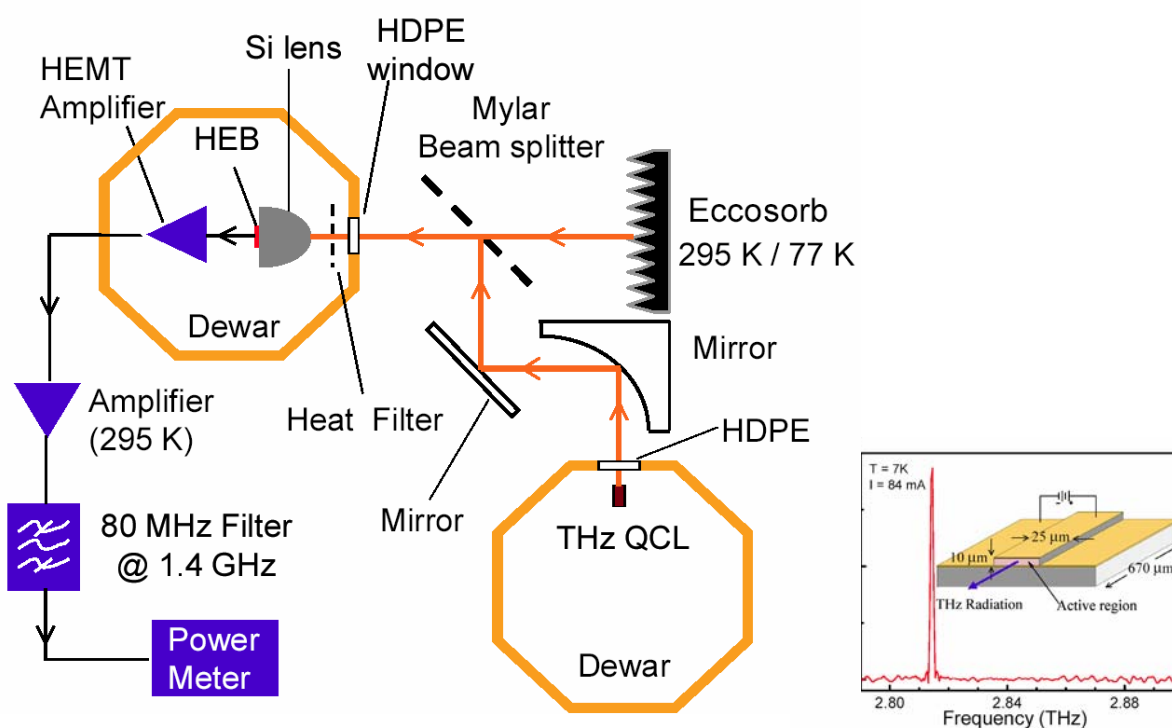


Figure 10. Schematic of the heterodyne receiver measurement set-up.

The key result of this work is demonstrated in Figure 11. A set of current versus voltage (I-V) curves of the HEB is shown for various levels (270, 300, 330 nW) of the effective power of radiation absorbed at the HEB, together with the receiver noise temperature, $T_{N,rec}$, as a function of voltage. (The inset shows a top view of the HEB with its spiral antenna). The power is varied by changing the DC current of the QCL, and the level is estimated by evaluating the absorbed power by the HEB through the isothermal technique. The noise temperature $T_{N,rec}$ is determined from the ratio of the IF output noise power for a hot and a cold load. Each set of $T_{N,rec}$ -V data shows a minimum region, indicating the optimum bias point. Best results are obtained for 300 nW LO power and 0.7 mV DC bias with $T_{N,rec}$ being as low as 1400 K, which is among the lowest obtained at this high frequency. This work, along with the phase-locking measurement described in the next section, has firmly established QCL's suitability in local-oscillator applications in a frequency range where no solid-state sources are available prior to our work.

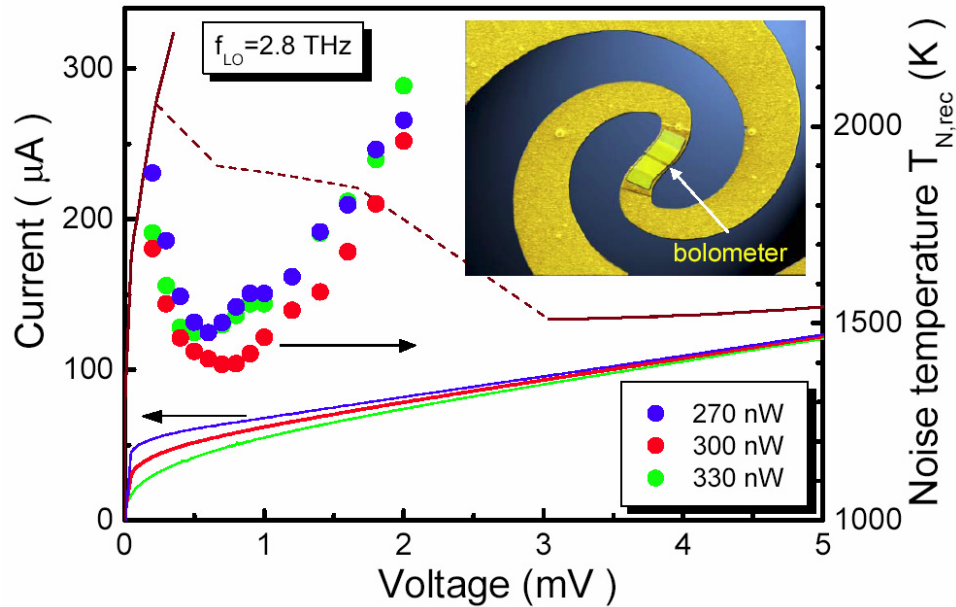


Figure 11. Current-voltage characteristics (solid line, left axis) of a NbN hot-electron bolometer (HEB) without and with radiation from a QCL at 2.814 THz. The measured receiver noise temperature $T_{N,rec}$ is shown as symbols (right axis) versus the bias voltage at different LO power levels. The inset shows a top view of the HEB with its spiral antenna.

Frequency and phase-lock control of THz quantum-cascade lasers

Sponsors

National Science Foundation
Grant ECS-0217782
NASA
Grant NNG04GC11G
AFOSR
Grant F49620-00-1-0331

Project Staff

Ben Williams, Sushil Kumar, and Qing Hu, in collaboration with A.L. Betz, R.T. Boreiko
Center for Astrophysics & Space Astronomy, University of Colorado, and Dr. John Reno at Sandia National Lab.

In this work, we have locked the frequency of a 3-THz quantum cascade laser (QCL) to that of a far-infrared gas laser with a tunable microwave offset frequency. The locked QCL lineshape is essentially Gaussian, with linewidths of 65 kHz and 141 kHz at the -3 dB and -10 dB levels, respectively. The lock condition can be maintained indefinitely, without requiring either temperature or bias current regulation of

the QCL. The result demonstrates that a terahertz QCL can be frequency controlled with 1 part in 10^8 accuracy, which is a factor of 100 better than that needed for a local oscillator in a heterodyne receiver for atmospheric and astronomical spectroscopy.

Figure 12 shows a schematic of the experimental apparatus. The outputs of the QCL and the FIR laser are combined by a wire grid polarizer and focused onto a room-temperature GaAs-Schottky-diode mixer in a corner reflector mount. The FIR line is the 3105.9368 GHz transition of methanol. Also incident on the mixer through its coaxial IF port is a 24.6 GHz signal that is produced by frequency doubling the output of a phase-locked YIG oscillator. The mixer generates a large number of sum and difference frequency terms from these inputs. The response of the diode is fast enough that sum frequency terms exceeding 6 GHz are produced, but for this experiment we are only interested in one 4th-order difference term that is the product of 4 AC electric fields.

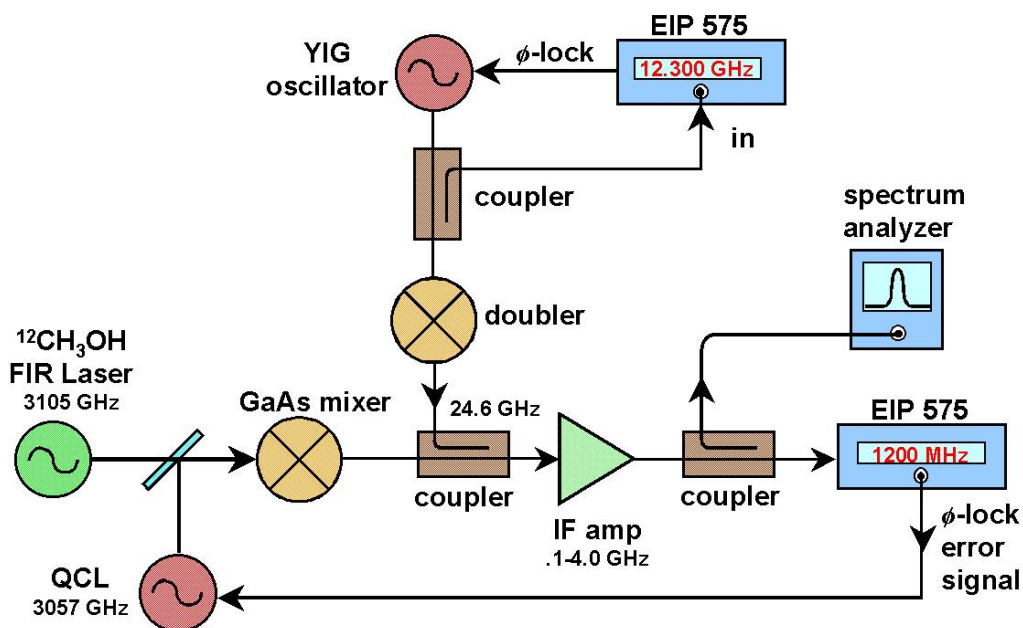


Figure 12. Diagram of Experimental Apparatus. The 24.6 GHz signal is injected into the coaxial IF port of the Schottky mixer by using a directional coupler backwards.

Figure 13a shows the phase-locked IF signal centered at 1200.000 MHz. The lineshape is essentially Gaussian. Figure 13b provides a closer view at line center, with a -3 dB bandwidth of 65 kHz and a -10 dB bandwidth of 141 kHz. This exact spectrum can be maintained indefinitely if the FIR laser cavity is re-peaked manually every 15 minutes.

In this work we have demonstrated that a THz QCL can be controlled with conventional phaselock techniques to have a long-term linewidth of 65 kHz and a frequency accuracy limited only by that of the reference oscillator, in this case a free-running FIR gas laser. This stability is already more than adequate for LO applications in remote sensing. In the near future it should be possible to lock the QCL to a harmonic of a microwave source which is itself referenced to a GPS-disciplined crystal oscillator. Such an arrangement would allow the QCL frequency to be controlled with 1 part in 10^{11} absolute accuracy. Currently, the 10 kHz loop bandwidth is a factor of 3×10^{-9} of the QCL operating frequency. This factor is small for oscillator stabilization by conventional microwave standards, and so it is not surprising that we see occasional excursions of the phase error that exceed $\pm\pi$. By modifying the EIP 575 circuitry, we

should be able to extend the loop bandwidth to 1 MHz and thereby achieve substantial additional narrowing of the QCL linewidth and perhaps approach the Schawlow-Townes linewidth of a few kHz.

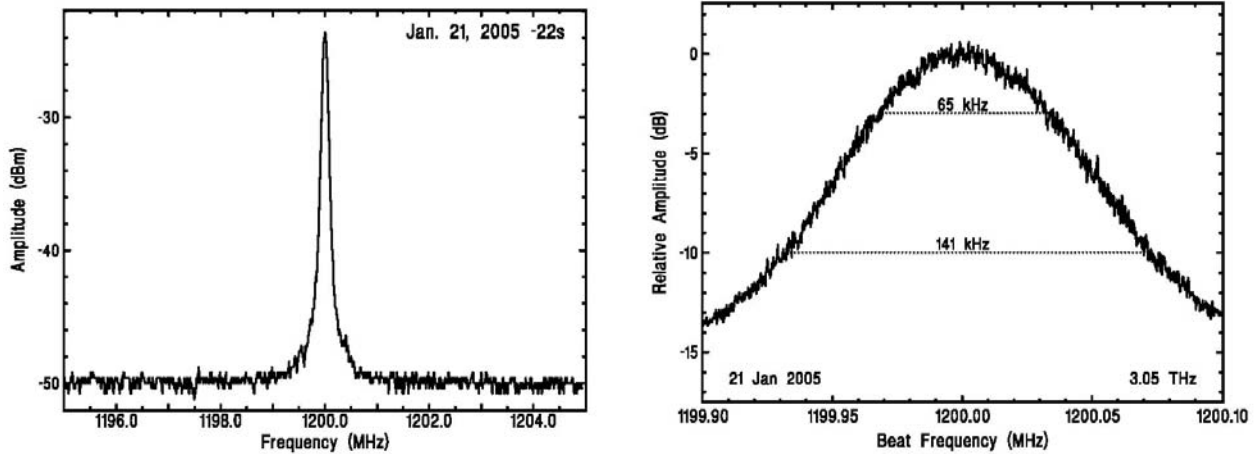


Figure 13. IF signal at 1200 MHz under locked conditions: (a) The frequency resolution of the spectrum analyzer is 100 kHz, and the post-detection video filter is on; (b) The plot shows a magnified view at line center with frequency resolution of 1 kHz, video filter on, and a scan time of 1 minute.

Real-time terahertz imaging using a microbolometer focal-plane array camera

Sponsors

National Science Foundation
 Grant ECS-0217782
 NASA
 Grant NNG04GC11G
 AFOSR
 Grant F49620-00-1-0331

Project Staff

Alan Lee and Qing Hu

Imaging using radiation in the terahertz frequency range, 0.3 THz to 10 THz, has demonstrated the ability to see the details within visibly opaque objects such as: integrated circuits packages, leaves, teeth, thin tissue samples, and illicit drugs in envelopes. The vast majority of THz imaging has been done by linearly scanning an object through a tightly focused THz beam – a practice which limits the acquisition time to the mechanical scan rate of the system. With upper limits of 100's of pixels/second for mechanical scanning, a complete image takes minutes to acquire.

Real-time imaging (30 frames per second or more) has previously been demonstrated by using an electro-optic crystal for frequency upconversion so that THz images can be viewed with a CCD focal-plane camera. However, this setup requires precise timing of the optical and THz pulses, necessitating a scanning delay mechanism, adding to its complexity. Furthermore, because of the short THz pulses (<1

ps), this scheme is inherently broadband (>1 THz). In applications such as the drug detection scheme, where detection of narrow-band fingerprint is required, a coherent narrow-band illumination source is crucial. Because of their compact sizes, many THz quantum-cascade lasers with different frequencies, corresponding to different chemical absorption bands, can be packaged tightly, forming a frequency agile coherent radiation source. In combination with a focal-plane imager, such a system can perform frequency-sensitive THz imaging at a rate far greater than the previous methods, allowing real-time THz monitoring and screening.

In this work, real-time, continuous wave (CW) terahertz imaging is demonstrated for the first time. The experimental arrangement is shown in Fig. 14. The terahertz beam is allowed to expand at the 1.4° divergence angle of the laser, over a path length of 1.5 m, resulting in a beam diameter of 4.5 cm. An off-axis paraboloid mirror ($f=10$ cm) and a germanium camera lens ($f=1$ cm, anti-reflection (AR) coated for $10\text{-}\mu\text{m}$ wavelength) are used to collimate the beam onto the focal-plane array. The image plane is located at 10 cm in front of the lens, just after the off-axis paraboloid mirror. At the image plane, a sample area of roughly 4×4 cm² is backlit and imaged onto the focal-plane array. A 6.5-mm thick sheet of high density polyethylene (2.4 dB insertion loss) is placed directly in front of the camera to provide a uniform background. Otherwise, the uneven $\sim 300\text{-K}$ ambient blackbody radiation will completely overwhelm the THz images, because of the high sensitivity (NETD ~ 40 mK) of the camera at $\sim 10\text{-}\mu\text{m}$ wavelength.

Fig. 14 also shows an image of a double edged razor blade, partially covered by a visibly opaque sheet of black low density polyethylene (LDPE, $50\ \mu\text{m}$ thickness, 1.1 dB insertion loss). The top picture shows a visible image of the covered razor blade in a metal frame, while the lower picture shows a single frame of real-time video of the same scene with THz radiation backlighting the razor blade. The acquisition time for this image was 16 ms. Even with signal averaging and a reduced number of illuminated pixels, the system still has an equivalent linear scan rate of 1.4×10^4 pixels/s, which is more than two orders of magnitude faster than a mechanically scanned system.

In the THz image, the detailed interior features and edges of the razor can be seen, as well as the contours of the black LDPE sheet. A contrast difference can also be seen between the uncovered and covered portions of the interior of the razor, due to the insertion loss of the black LDPE. The resolution for the system can be compared to the Rayleigh criterion, which states that the minimum resolvable angle is: $\theta \approx 1.22\lambda/d$, where λ is the wavelength, and d is the 1-cm diameter of the germanium camera lens. At the image plane, which is 10 cm in front of the lens, the Rayleigh criterion limits the resolution to ~ 1.5 mm. The 2-mm features (marked in part (a)) of the razor are resolvable, indicating a near diffraction-limited optics. It should be stressed that since human eyes are more sensitive to moving objects, the real-time images of a moving target displayed on a monitor are more impressive than the still image of Fig. 14 suggests. The capability of performing real-time video imaging at a specific THz frequency is what distinguishes this system from all the other THz imaging systems reported in literature.

This work is only the first step demonstrating the feasibility of real-time THz imaging using a coherent CW illumination source. Significant improvements in SNR and spatial resolution can be made by designing focal-plane microbolometer cameras specifically optimized for THz frequencies. These include using different radiation absorbing materials, correctly placing the reflecting $\lambda/4$ backplane, and using appropriate AR coatings and a larger-size, slower focus lens. In combination with a multi-color QCL illumination source, we envision a compact system that can perform frequency-sensitive THz imaging in real time.

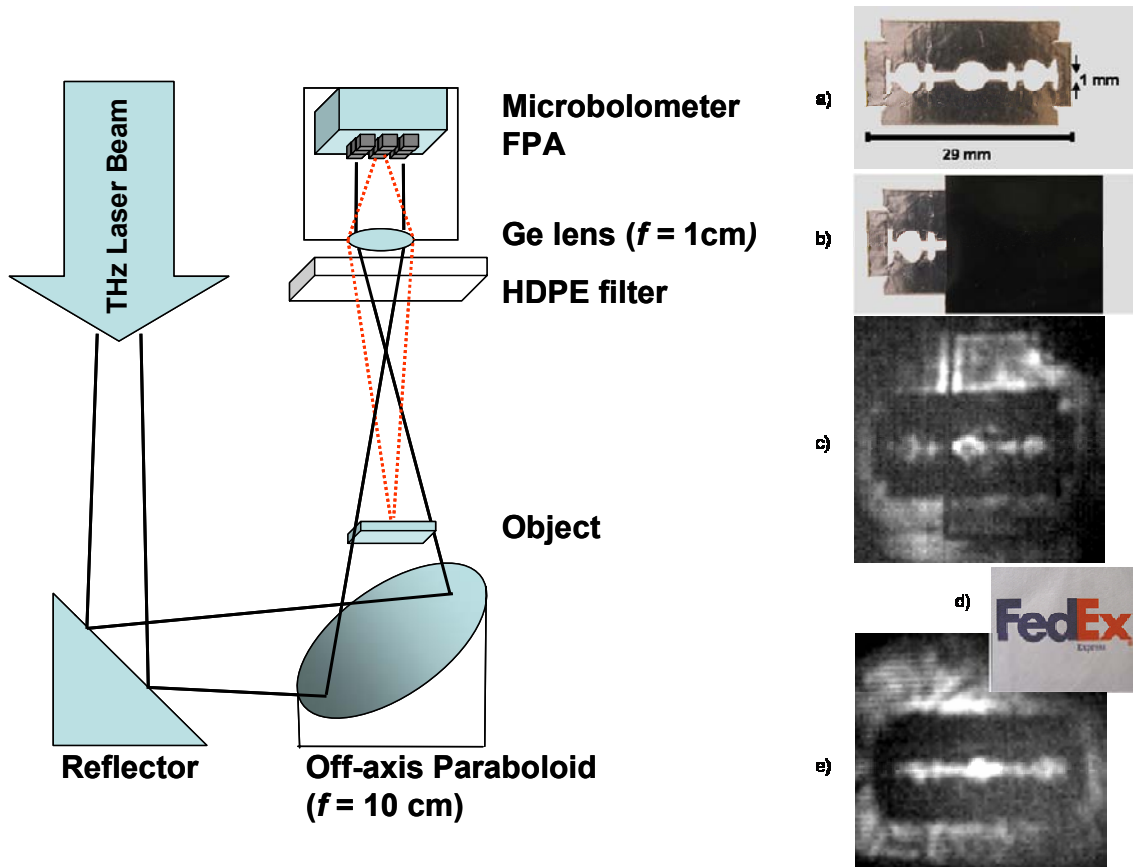


Figure 14. Left: Experimental Setup: the solid lines show the path of the THz beam; the broken lines show the marginal rays of the camera lens which are focused at a point on the object. Right: Visible and terahertz images of scaled razor blade: (a) visible image ; (b) visible image partially obscured by a blackened low density polyethylene sheet; (c) same scene as (b) shown at 2.52 THz , taken with 16-ms acquisition time and histogram adjusted; (d) a sample of a FedEx envelope (made from DuPont Tyvek, a fibrous HDPE material); (e) razor blade completely inside a FedEx envelope at 2.52 THz, taken with 5-s acquisition time and histogram adjusted.

Development of mid-infrared (8-12 μm wavelength) quantum-cascade lasers

Sponsors

Army Research Office SBIR program

Project Staff

Sushil Kumar and Qing Hu, in collaboration with J. Joseph and N. Samal at Trion Technology, Tempe, AZ.

The mid-infrared frequency range of 8-12 μm wavelength is one of the most important spectral range for military applications. The atmosphere is highly transparent in this range, which also coincides with the peak wavelength of blackbody radiation at ambient 300-K temperature. Consequently, compact and powerful solid-state lasers operating in this frequency range could be quite useful in free-space communications and countermeasures. In the Phase I of this Army-sponsored project, we have designed three QCL structures based on different design principles, with their description and band diagrams shown below.

Superlattice based active and injector regions: In this type of design, as shown in Fig. 15(a), two superlattice conduction bands (minibands) are created in the quantum wells and the optical transition occurs from the bottom of the upper miniband to the top of the lower miniband. The photon energy corresponds to that of the energy gap (minigap) between the two minibands. This type of design is characterized by a vertical optical transition and hence a large oscillator strength. Electron injection occurs through interminiband tunneling in the strongly coupled superlattices. The lifetime of the lower radiative state is kept ultrashort by intraminiband electron-phonon and electron-electron scattering in the lower miniband and hence population inversion is easier to achieve. This process is aided by the large phase space that is available to the electrons in the lower radiative state to scatter into. Superlattice-based active and injector /relaxation regions also have a higher current carrying capability (without running into level misalignment at higher current densities) and hence these designs can achieve higher peak optical power levels. To avoid electric field induced localization of superlattice states a flat miniband profile is obtained by compensating the applied electric field with an effective quasidelectric field generated by “chirping” the superlattice period (gradual variation of the superlattice period length).

Bound-to-continuum transition based active region: As shown in Fig. 15(b), an active region spanning the whole superlattice period characterizes this type of design. It consists of a chirped superlattice forming a tilted lower miniband, which is widest in the center and narrows close to the injection barrier. The upper radiative state is a single state created in the first minigap by a small well adjacent to the injection barrier. Its wavefunction is the maximum close to the injection barrier and decreases smoothly in the active region. This state is well separated from the other high lying states in the superlattice and hence there is no need for separate active and injector /relaxation regions. Electrons are injected into the upper radiative state by resonant tunneling through the injection barrier with high injection efficiency. The lower radiative state in the top of the lower miniband has an ultrashort lifetime due to fast intraminiband scattering as in the superlattice-based designs. The optical transition is slightly diagonal that minimizes the coupling of the injector levels to the states of the lower miniband hence achieving a more selective injection into the upper radiative state even at higher temperatures.

Two-phonon resonance based active region: As shown in Fig. 15(c), this type of design shares its upper radiative state geometry with the design based on a bound-to-continuum transition and hence achieves higher injection efficiency into the upper radiative state, which is characteristic of the designs based on resonant tunneling principle. The design differs in the technique by which electrons are extracted from the lower radiative state. Efficient electron depopulation of the lower radiative state occurs via a ladder of three coupled states separated by a longitudinal optical phonon energy each through ultrafast electron-phonon scattering mechanism. This has been shown to perform significantly better than the original three quantum well QCL design with a ladder of just two states as compared to three. The lower radiative state lifetime thus obtained is comparable to those of superlattice based designs.

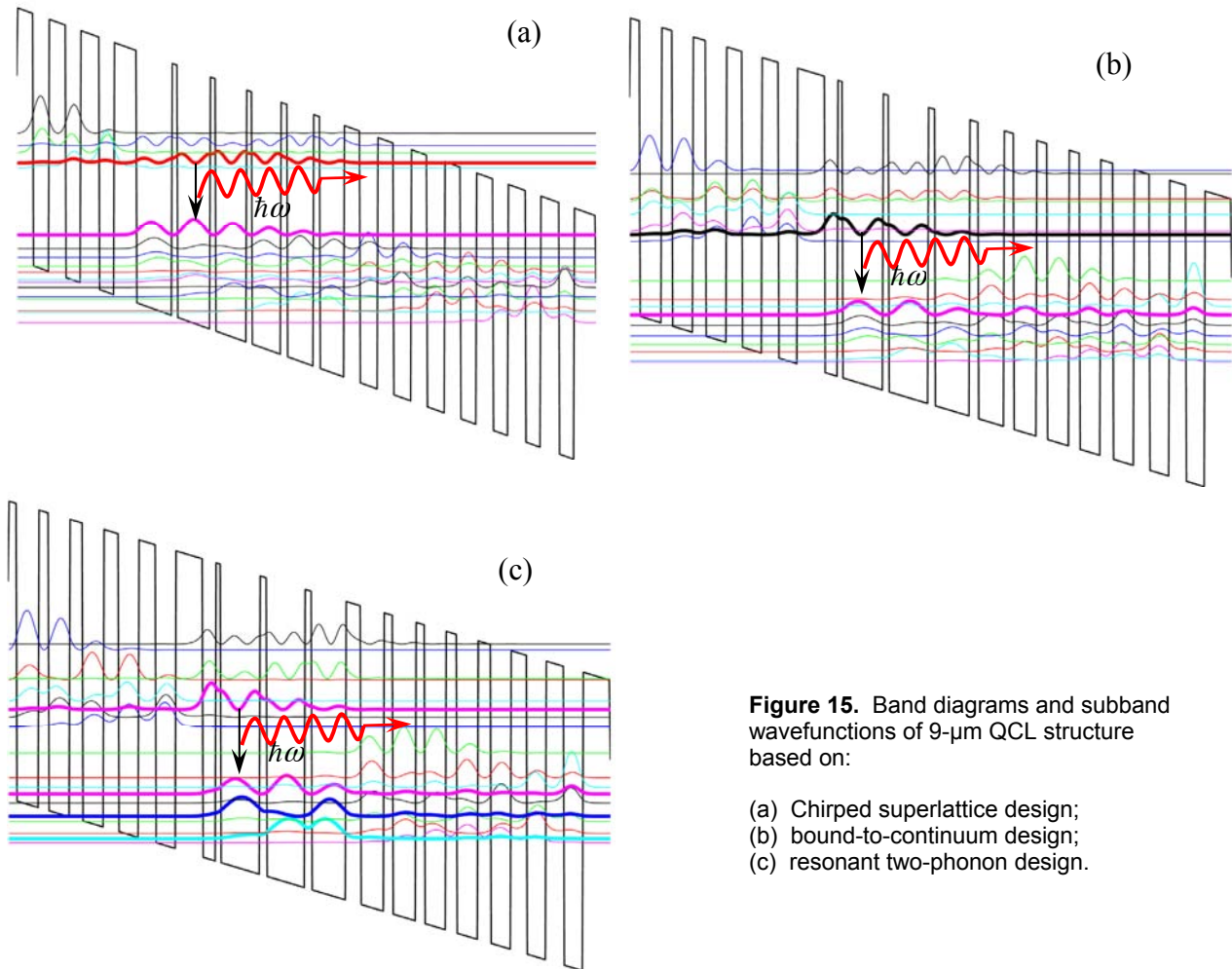


Figure 15. Band diagrams and subband wavefunctions of 9- μm QCL structure based on:

- (a) Chirped superlattice design;
- (b) bound-to-continuum design;
- (c) resonant two-phonon design.

Patent applications, Publications, and Conference Presentations

1. H. Callebaut, S. Kumar, B. S. Williams, Q. Hu, and J. L. Reno, "Importance of electron-impurity scattering for electron transport in THz quantum-cascade lasers," *Appl. Phys. Lett.* **84**, 645 (2004).

Chapter 27. Terahertz Quantum Cascade, Electronics, and Real-time Imaging

2. S. Kumar, B. S. Williams, S. Kohen, Q. Hu, and J. L. Reno, "Continuous-wave operation of terahertz quantum-cascade lasers above liquid-nitrogen temperature," *Appl. Phys. Lett.* **84**, 2494 (2004).
3. B. S. Williams, S. Kumar, Q. Hu, and J. L. Reno, "Resonant-phonon terahertz quantum-cascade laser operating at 2.1 THz ($\lambda \approx 141 \mu\text{m}$)," *Elect. Lett.* **40**, 431 (2004).
4. Hu, Q., B. S. Williams, S. Kumar, H. Callebaut, and J. L. Reno, "Phonon-Depopulated THz Quantum Cascade Lasers," pp. 319-329, *Future Trend in Microelectronics: The Nano, the Giga, and the Ultra*, S. Luryi, J. Xu, A. Zaslavsky, eds., John Wiley & Sons, New York, 2004.
5. Q. Hu, B. S. Williams, S. Kumar, H. Callebaut, S. Kohen, and J. L. Reno, "Resonant-phonon-assisted THz Quantum Cascade Lasers with Metal-metal Waveguides," to be published in a Topical Issue on TERAHERTZ TECHNOLOGY, *Journal of Semiconductor Science and Technology*, (2005).
6. S. Kohen, B. S. Williams, and Q. Hu, "Electromagnetic modeling of terahertz quantum cascade laser waveguides and resonators," *J. Appl. Phys.* **97**, 053106 (2005).
7. M. S. Vitiello, G. Scamarcio, B. S. Williams, S. Kumar, Q. Hu, and J. L. Reno, "Measurement of subband electronic temperatures and population inversion in THz quantum cascade lasers," *Appl. Phys. Lett.* **86**, 111115 (2005).
8. J. R. Gao, J. N. Hovenier, Z. Q. Yang, J. J. A. Baselmans, A. Baryshev, M. Majenius, T. M. Klapwijk, A. J. L. Adam, T. O. Klassen, B. S. Williams, S. Kumar, Q. Hu, and J. L. Reno, "A terahertz heterodyne receiver based on a quantum cascade laser and a superconducting bolometer," to be published *Appl. Phys. Lett.*, (2005).
9. H. C. Liu, M. Wächter, D. Ban, Z. R. Wasilewski, M. Buchanan, G. C. Aers, J. C. Cao, S. L. Feng, B. S. Williams, and Q. Hu, "Effect of doping concentration on the performance of terahertz quantum-cascade lasers," submitted to *Appl. Phys. Lett.* (2005).
10. A. L. Betz, R. T. Boreiko, B. S. Williams, S. Kumar, Q. Hu, and J. L. Reno, "Frequency and Phaselock Control of a 3-THz Quantum Cascade Laser," to be published in *Opt. Lett.* (2005).
11. A. W. M. Lee and Q. Hu, "Real-Time, Continuous-Wave Terahertz Imaging using a Microbolometer Focal-Plane Array," submitted to *Opt. Lett.* (2005).
12. B. S. Williams, S. Kumar, Q. Hu, and J. L. Reno, "Operation of terahertz quantum-cascade lasers at 164 K in pulsed mode and at 117 K in continuous-wave mode," *Optics Express*, **13**, 3331-3339 (2005).
13. Q. Hu, "Resonant-phonon-assisted THz quantum-cascade lasers using metal-metal waveguides for mode confinement," International Workshop on Quantum Cascade Lasers, Servile, Spain, January 4-7, (2004). (Invited)
14. B. S. Williams, S. Kumar, H. Callebaut, S. Kohen, Q. Hu, and J. L. Reno, "Terahertz quantum cascade lasers using resonant-phonon depopulation and metal-metal waveguides," IEEE Photonics West, San Jose, CA, January 27 (2004). Published in *SPIE Proceedings*, vol. xxx, yyy (2004). (Invited)
15. Q. Hu, "Terahertz Quantum Cascade Lasers," DOE-NSF-NIH Workshop on Opportunities in THz Science, February 12-14, 2004, Sheraton National Hotel – Arlington, VA.
16. Hu, Q., "Terahertz Quantum-cascade Lasers," presented at the 2004 APS March meeting in session Y2.004, Montreal, Canada, March (2004). (Invited)
17. A.L. Betz, R.T. Boreiko, B. S. Williams, S. Kumar, Q. Hu, and J. L. Reno, "A Phase-locked Terahertz Quantum Cascade Laser," presented at the 15th International Symposium on Space Terahertz

- Technology, Northampton, Massachusetts, April (2004), published in the symposium proceedings, pp (2004).
18. Hu, Q., "Terahertz Quantum-cascade Lasers," presented at the 2nd International Symposium on Ultrafast Phenomena and Terahertz Waves, Shanghai, China, May (2004). (Invited)
 19. B. S. Williams, S. Kumar, Q. Hu, and J. L. Reno, "Resonant-phonon terahertz quantum cascade lasers at long wavelengths," session CMZ1, CLEO/QELS 2004, San Francisco, CA, May (2004).
 20. S. Kumar, B. S. Williams, S. Kohen, Q. Hu, and J. L. Reno, "High temperature continuous-wave operation of terahertz quantum cascade lasers," session CMZ2, CLEO/QELS 2004, San Francisco, CA, May (2004).
 21. Q. Hu, "Terahertz Quantum Cascade Lasers," presented at the 6th International Conference on Mid-infrared Optoelectronics Materials and Devices (MIOMD-VI), St. Petersburg, Russia, June (2004). (Invited)
 22. Miriam S. Vitiello, Vincenzo Spagnolo, Gaetano Scamarcio, Cinzia Di Franco, Benjamin S. Williams, Sushil Kumar, Qing Hu, John. L. Reno, "Electronic and lattice temperatures of terahertz quantum cascade lasers based on phonon-assisted depopulation," presented at the 6th International Conference on Mid-infrared Optoelectronics Materials and Devices (MIOMD-VI), St. Petersburg, Russia, June (2004).
 22. Miriam S. Vitiello, Vincenzo Spagnolo, Gaetano Scamarcio, Cinzia Di Franco, Michele Sibilano, Benjamin S. Williams, Sushil Kumar, Qing Hu, John. L. Reno, "Measurement of the electron - lattice coupling in terahertz quantum cascade lasers," presented at INFMeeting 2004, Italy, June (2004).
 23. B. S. Williams, S. Kumar, H. Callebaut, Q. Hu, and J. L. Reno, "Resonant-phonon terahertz quantum cascade lasers using metal-metal waveguides," The 29th International Conference on Infrared and Millimeter Waves and the 12th IEEE International Conference on Terahertz Electronics (IRMMW2004/THz2004), Karlsruhe, Germany, September 27, (2004). (Invited)
 24. Q. Hu, "Terahertz Quantum Cascade Lasers," 2004 Workshop on Frontiers in Electronics (WOFE'04), Aruba, December 21 (2004).
 25. Q. Hu, "Terahertz Quantum Cascade Lasers," 8th International Symposium on Contemporary Photonics Technology (CPT2005), Tokyo, Japan, January 13, (2005). (Invited)
 26. B. S. Williams, S. Kohen, S. Kumar, Q. Hu, and J. L. Reno, "Terahertz quantum cascade lasers with metal-metal waveguides," IEEE Photonics West, San Jose, CA, January 25 (2005). Published in SPIE Proceedings, vol. **xxx**, yyy (2005). (Invited)
 27. Q. Hu, "Terahertz Quantum Cascade Lasers," Princeton BMD/OOE seminar (Electronics Devices & Materials, Opto & Optoelectronics), Princeton University, NJ, March 7 (2005). (Invited)
 28. A.J.L. Adam, J. N. Hovenier, and T.O. Klaassen, M. Hajenius, J.R. Gao, B. S. Williams, S. Kumar, Q. Hu, and J. L. Reno, "Evaluation of a Quantum Cascade Laser as Local Oscillator for Heterodyne Detection of THz Radiation," OSA topical meeting on Optical Terahertz Science and Technology, Orlando, FL, March 15, (2005).
 29. B. S. Williams, S. Kumar, H. Callebaut, S. Kohen, Q. Hu, and J. L. Reno, "Advances in Terahertz Quantum-Cascade Lasers Using Metal-metal Waveguides," OSA topical meeting on Optical Terahertz Science and Technology, Orlando, FL, March 15, (2005).
 30. A. L. Betz, R. T. Boreiko, B. S. Williams, S. Kumar, Q. Hu, and J. L. Reno, "Frequency and Phaselock Control of a 3-THz Quantum Cascade Laser," OSA topical meeting on Optical Terahertz Science and Technology, Orlando, FL, March 15, (2005).

31. Q. Hu, "Terahertz Quantum Cascade Lasers," Harvard EE seminar, Harvard University, MA, April 8 (2005). (Invited)
32. Q. Hu, "Terahertz Quantum-cascade lasers as local oscillators," 16th International Symposium on Space Terahertz Technology (ISSTT 2005), Göteborg, Sweden, May 2-4 (2005). (Invited)
33. A.J.L. Adam, J.N. Hovenier, I. Kasalynas, T.O. Klaassen, J.R. Gao, B.S. Williams, S. Kumar, Q. Hu, E.E. Orlova, and J. L. Reno, "Near and Far Field Beam Pattern Measurements on Quantum Cascade Lasers Operating at 2.8 THz," 16th International Symposium on Space Terahertz Technology (ISSTT 2005), Göteborg, Sweden, May 2-4 (2005).
34. Q. Hu, "Terahertz Devices," Workshop On Compound Semiconductor Devices & Integrated Circuits in Europe (WOCSDICE2005), Cardiff, UK, May 15-18 (2005). (Invited)
35. Q. Hu, "Terahertz Quantum Cascade Lasers," CLEO/QELS 2005, Baltimore, Maryland, May 22-27 (2005). (Invited)
36. Miriam Serena Vitiello, Gaetano Scamarcio, Vincenzo Spagnolo, Benjamin S. Williams, Sushil Kumar, Qing Hu, and John L. Reno, "Hot electrons in resonant-phonon terahertz quantum cascade lasers," CLEO/QELS 2005, Baltimore, Maryland, May 22-27 (2005).
37. Q. Hu, "High-temperature operation of THz quantum-cascade lasers," CLEO Europe 2005, Munich, Germany, June 12-17 (2005). (Invited)
38. Q. Hu, "THz quantum cascade lasers," 35th Workshop: Physics and Technology of THz Photonics, International School of Solid State Physics, Erice, Italy, July 20-26, (2005). (Invited)
39. Qing Hu and Alan Wei Min Lee, "Terahertz Imaging Devices," patent pending, M.I.T. Case No. 11528 (2005).
40. B. S. Williams, S. Kumar, Q. Hu, and J. L. Reno, "Distributed-feedback terahertz quantum-cascade lasers using laterally corrugated metal waveguides," submitted to Opt. Lett. (2005).

Theses

Ph.D. thesis

Konistis, Konstantinos, thesis title, "A Heterojunction Bipolar Transistor with Stepwise Alloy-Graded Base: Analysis, Design, Fabrication, and Characterization," August, 2004.

M.S. thesis

Stephen Michael Kohen, thesis title, "Electromagnetic Modeling of Terahertz Quantum Cascade Laser Waveguides and Resonators," May 2004.